Additive Manufacturing 73 (2023) 103647

Contents lists available at ScienceDirect

Additive Manufacturing

journal homepage: www.elsevier.com/locate/addma

Designing an Fe-Ni-Ti maraging steel tailor-made for laser additive manufacturing

Philipp Kürnsteiner[a,b,*], Pere Barriobero-Vila[c,d], Priyanshu Bajaj[a,e], Frédéric De Geuser[f], Markus B. Wilms[g,h], Eric A. Jägle[a,i], Dierk Raabe[a]

[a] Department Microstructure Physics and Alloy Design, Max-Planck-Institut für Eisenforschung GmbH, Düsseldorf 40237, Germany
[b] Christian Doppler Laboratory for Nanoscale Phase Transformations, Center for Surface and Nanoanalytics, Johannes Kepler University Linz, Linz 4040, Austria
[c] Technical University of Catalonia (UPC), Department of Materials Science and Engineering, Eduard Maristany Av. 16, 08019 Barcelona, Spain
[d] CIM UPC, Carrer de Llorens i Artigas 12, 08028 Barcelona, Spain
[e] m4p material solutions GmbH, Gewerbestraße 4, Feistritz im Rosental 9181, Austria
[f] University Grenoble Alpes, CNRS, Grenoble INP, SIMAP, F-38000 Grenoble, France
[g] Fraunhofer Institute for Laser Technology ILT, Aachen 52074, Germany
[h] Chair of Materials Science and Additive Manufacturing, School of Mechanical Engineering and Safety Engineering, University of Wuppertal, 42119 Wuppertal, Germany
[i] Institute of Materials Science, Universität der Bundeswehr München, Neubiberg 85579, Germany

ARTICLE INFO

Keywords:
Additive manufacturing
Alloy design
Maraging steel
Directed energy deposition (DED), Atom probe tomography (APT), High-energy X-ray diffraction (HEXRD)

ABSTRACT

Laser additive manufacturing (LAM) offers high flexibility in the production of customized and geometrically complex parts. The technique receives great interest from industry and academia but faces substantial challenges regarding processability and insufficient mechanical properties of LAM-produced material. One reason is that currently mainly conventional alloys are being used in LAM, which were developed for different processes such as casting. Since these alloys are not optimized for the specific process conditions encountered in LAM such as fast cooling and cyclic re-heating, they cannot be expected to perform ideally in such processes regarding processability and resulting mechanical properties. Here we present the development of a new, simple ternary Fe-Ni-Ti maraging-type alloy tailor-made for LAM. We used compositionally graded samples to screen Ti compositions from 0 to 21 at. % and efficiently identify promising microstructures and mechanical properties. Under LAM solidification conditions the desired mainly martensitic microstructure needed for a maraging steel formed at Ti compositions ranging from 0 to 7 at. %. Within this composition range, the intended microstructure is formed and additionally some unique process conditions of LAM such as cyclic re-heating can be exploited. Specifically, in-situ phase transformations can be controlled during LAM, via the thermal history. At higher Ti compositions two different eutectic microstructures with different primary phases were found that show a high hardness of up to 700 HV.

1. Introduction

Laser additive manufacturing (LAM) enables the production of complex, customized parts by melting and consolidating metallic powder with a focused laser beam. Three-dimensional parts can be printed directly from a computer aided design (CAD) model in a near net shape manner by sequentially adding material layer by layer [1–5]. One of the most prominent LAM techniques is directed energy deposition (DED), which uses a feeding nozzle to introduce the metal powder into a melt pool via an inert carrier gas. The powder is completely melted and forms fully dense parts upon solidification. LAM has emerged from a pure prototyping technique to a manufacturing process to produce high-end parts in many industrial sectors such as aerospace [6–9], tool making industry [10–13] or the biomedical sector [14–18]. Additive manufacturing is often regarded as a disruptive technology that could revolutionize manufacturing [19,20]. However, the metal LAM industry faces problems regarding either insufficient mechanical properties of well printable, but soft alloys or poor processability (leading to pores, cracking, bad surface quality etc.) of high strength alloys. Materials with high mechanical strength such as carbon bearing tool steels or 7XXX

---

* Corresponding author at: Department Microstructure Physics and Alloy Design, Max-Planck-Institut für Eisenforschung GmbH, Düsseldorf 40237, Germany.
E-mail addresses: philipp.kuernsteiner@jku.at, p.kuernsteiner@mpie.de (P. Kürnsteiner).

https://doi.org/10.1016/j.addma.2023.103647
Received 14 December 2022; Received in revised form 17 May 2023; Accepted 7 June 2023

series aluminum often show severe cracking during LAM [21–25]. Their well printable “counterparts” such as stainless steels or Al-Si alloys do not possess the mechanical strength required for demanding applications such as tools or structural parts [26–31]. A major reason for these problems is that currently LAM is often applied to conventional alloys which were developed for completely different processes such as casting or rolling. Hence there is a great need to develop new alloys tailor-made for AM. These new alloys must avoid the problems encountered with conventional compositions such a cracking but ideally should also exploit some of the new capabilities and features of LAM processes, such as rapid cooling and cyclic re-heating.

One such feature is the unique thermal history of every material processed by LAM: after rapid quenching from the liquid state, consolidated material experiences a cyclic re-heating when neighboring tracks and subsequent layers are created [32–34]. This repeated heating is often termed intrinsic heat treatment (IHT) [35–40]. The effect of the IHT on the microstructure of LAM-produced parts has been studied in various different alloys including Ni-based superalloys [40], Ti-6Al-4V [41–44], Al-Sc alloys [45,46], and steels [34,38,39,47–49]. In our previous study, we demonstrated how the IHT can be used to trigger solid-state phase transformations in a simple ternary Fe-Ni-Al maraging-type steel specifically designed to respond to the IHT during DED with quick precipitation kinetics [35,36]. Specifically, the IHT caused an extremely high number of NiAl nano-precipitates in a Ni-martensitic matrix and in-situ precipitation strengthened the material. For in-situ precipitation hardening to work, fast precipitation kinetics are needed in order to obtain significant precipitation during the short temperature spikes of the IHT. Additionally, to the previously mentioned Fe-Ni-Al alloy system, also Fe-Ni-Ti shows very fast precipitation kinetics [50–52]. An advantage of the Fe-Ni-Ti system compared to the previously studied Fe-Ni-Al system is its lower martensite start temperature M_s that is readily accessible in DED processes (e.g. below 200 °C for an Fe19Ni5Ti (wt. %) steel). This allows controlling martensite transformation via the process parameters during the DED process [53]. Having access to both solid-state phase transformations, namely martensite transformation and precipitation, via the thermal history during LAM allows to locally control the microstructure and mechanical properties.

Fe-Ni-Ti is a simple ternary model maraging steel. This class of steels is of great importance in tooling, aerospace and energy industries due to its combination of high strength, toughness and ductility [54–56]. Conventional maraging steels feature a soft Ni martensitic microstructure which is hardened by a high density of intermetallic precipitates. Conventionally as well as LAM-produced commercial maraging steels need to undergo an aging heat treatment to form these precipitates and to develop the final strength of the material [47,56–60]. Typical intermetallic precipitates to form during aging include NiAl (β´-phase), Ni_3Ti (η-phase), Fe_2Mo (Laves-phase) and Ni_2AlTi [56,61].

Maraging steels are well suited for LAM due to their excellent processability/weldability as a consequence of their low C content compared to other tool steels. LAM-produced maraging steels show a cellular dendritic solidification structure with a mainly martensitic microstructure but also contain a significant fraction of retained austenite as a result of microsegregation at interdendritic (intercellular) regions [35,57,58,62,63].

Here, we present an approach to develop a new alloy that is tailor-made for LAM, making use of the rapid alloy prototyping (RAP) capabilities of DED. As a nozzle-based LAM process, it enables changing the chemical composition of deposited materials during the manufacturing process using multiple powder feeders and in-situ mixing of the powders from these feeders [64]. Using this methodology, we produced a compositionally graded sample of a simple ternary maraging-type Fe-Ni-Ti steel with Ti compositions ranging from 0 to 21 at. % (i.e. alloys of the type $[\text{Fe-19Ni}]_{1-x}\text{-Ti}_x$ with $0 < x < 21$ at. %). On this single sample we could efficiently screen different Ti compositions and identify the most promising ones for further investigations. Specifically, here we were looking for compositions that result in the desired (i.e. mainly martensitic) microstructure for a maraging steel after the LAM process. It should be noted that this work focuses on the microstructures found at different Ti compositions. How the IHT can be exploited to control phase transformations and in-situ precipitation hardening in the region of the desired martensitic microstructure (e.g. Fe19Ni5Ti (at. %)) has been described in detail in a previous publication [53].

2. Materials and methods

2.1. Additive manufacturing

Samples for this study were produced by directed energy deposition (DED) using a 5-axis handling system and a fiber coupled diode laser system LDM 3000–60 (Laserline GmbH, Mülheim-Kärlich, Germany) which has a specific wavelength of 976 nm and a beam parameter product of 60 mm.mrad. We used a final beam spot size of 1.8 mm generated by a collimation- and focusing lens with a focal lengths of 65 mm and 195 mm, respectively. Metal powder is fed to the powder nozzle from two independent containers of the used disc-based feeding systems Sulzer Metco Twin 10 C (OC Oerlikon AG, Pfäffikon, Switzerland).

We used Argon atomized Fe19Ni (at. %) (Nanoval GmbH & Co. KG, Berlin, Germany) and pure Ti powder material (TLS Technik GmbH & Co. KG, Bitterfeld, Germany), both sieved to the particle size fraction of 45–90 μm. One of the powder containers was filled with pre-alloyed Fe19Ni (at. %) powder and was mixed with different amounts of Ti (99.9 % purity) powder from the other container. To manufacture the compositionally graded Fe19Ni-xTi sample (specifically a $[\text{Fe-19Ni}]_{1-x}\text{-Ti}_x$ alloy with $0 < x < 21$ at. %) for this study, varying Ti compositions were achieved by adjusting the rotation speed of the discs in both powder containers. Hence, the desired mixture of metal particles and consequently of the final composition of each layer of the bulk volume is acquired. The output of the Ti feeder is increased by 0.1 rpm after each layer, starting with 0 rpm in the first layer. The output of the Fe19Ni (at. %) feeder is kept constant at 1.5 rpm in every layer. This approach results in the desired compositional gradient along the build direction (BD) of the sample. According to the setup described in [35], the carrier gas streams from both feeding containers are combined to a single stream by a Y-piece before entering the 3- way nozzle (Fraunhofer Institute for Laser Technology, Aachen, Germany) and finally the melt pool. It shall be pointed out that the Fe-19Ni powder and Ti powder is mixed already in the Y-piece i.e. before entering the melt pool. The Y-piece is made from stainless steel and connects the two tubes (inner diameter: 4 mm) containing the powder-gas streams from both powder containers to form a single powder-gas stream in a tube (inner diameter: 4 mm). It additionally allows effective mixing of both powder materials before entering a diffusor unit to split the single powder-gas stream into three individual powder-gas streams to feed the used 3-way nozzle. The used cone-shaped nozzle contains three injectors aligned in 120° angles, allowing the conversion of the 3 individual powder-gas streams from the injectors below the nozzle’s tip in a fixed distance of 12 mm. Argon is used as both carrier gas and as shielding gas to prevent oxidation reactions of the melt pool with atmospheric air.

We used a bidirectional scan strategy, depositing 14 single tracks next to each other with a constant track offset of 900 μm. In total 22 layers were deposited with a constant height offset of 600 μm between layers. A laser power of 910 W and a deposition speed of 600 mm/min were used and kept constant for every layer. The sample was built on a 1.2365 (AISI H10) steel substrate plate. We selected a low alloyed steel so that the only significant contamination to the sample is Fe. We looked for contaminations of e.g. Cr in the sample but could not detect any contamination at all. We see a clear Cr signal in the EDS line scan in the substrate plate but it drops to noise level exactly at the interface to the sample.

2.2. Characterization methods

Standard metallographic techniques including grinding with SiC paper and a finishing step with colloidal silica suspension (OPS) were used to prepare the sample for microstructure characterization. For light optical microscopy (LOM), the polished sample was etched using 5 vol. % Nital (HNO_3 in ethanol). Owing to the graded composition (i.e. Ti contents from 0 to 20 at. %), it is difficult to find an etching time that works perfectly for the entire sample without over-etching the top part, or under-etching the bottom part. The condition we chose for the LOM micrograph shown here is such that the bottom part is slightly under-etched. Although the top part is etched rather heavily, it allows the visualization of the two different eutectic microstructures. The LOM micrograph is meant to serve as an overview guideline for the transition positions from one microstructure regime to another. The definition of the 3 main microstructure regimes is given in Fig. 1. The detailed analysis of the microstructure was performed using electron microscopy.

A ZEISS Merlin was used for scanning electron microscopy (SEM) based characterization including energy-dispersive X-ray spectroscopy (EDS). Backscattered electron (BSE) and secondary electron (SE) imaging was used to obtain the corresponding SEM micrographs. EDS was performed at an acceleration voltage of 15 kV using a Bruker QUANTAX detector. $K\alpha$ lines for all elements were used for quantification.

A Zwick Roell ZHV 10 was used to perform Vickers hardness measurements with a load of 0.5 kg along the DED deposited layers of the Ti graded specimen, resulting in a hardness profile as a function of specimen height (i.e. Ti content). A minimum of 6 indents were performed within each layer. The mean hardness values plus standard deviation for each layer are shown.

Atom probe tomography (APT) experiments were performed in a Cameca LEAP 5000X HR and a LEAP 5000 XS in laser mode. Pulse frequencies of 333–625 kHz and 125–250 kHz were used together with detection rates of 2–3 % and 1.5–1.7 % for the XS and the HR device, respectively. Temperatures between 40 K and 50 K and laser energies

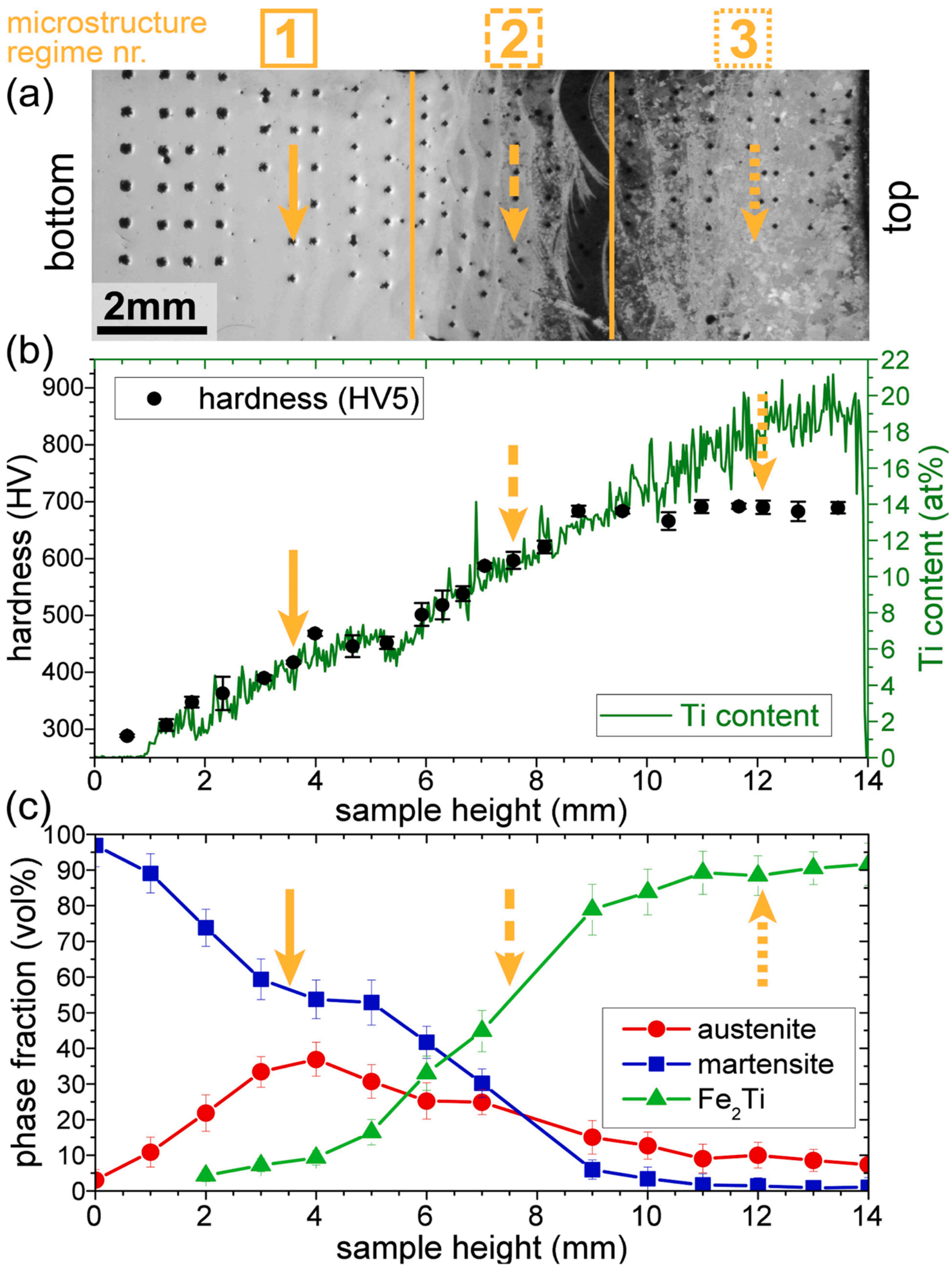

Fig. 1. Overview of the Ti graded specimen produced by DED for this study. (a) is a light optical micrograph after Nital etching. The different microstructure regimes that occur at low, intermediate and high Ti contents are separated by vertical orange lines and indicated by numbers. The regular array of dark spots corresponds to the indents from hardness measurements. Orange arrows in this figure mark the locations (i.e. corresponding Ti compositions) for the in-depth microstructure characterization described in Section 3.2. (b) shows the Ti composition from SEM-EDS quantification as a function of the sample height overlaid with hardness. The increase in Ti content along the sample build height is accompanied by a steep increase in hardness up to 14 at. % Ti where a plateau in hardness at around 700 HV is reached. (c) depicts the phase composition obtained by synchrotron HEXRD along the sample height. Starting from an almost fully martensitic microstructure at low Ti contents, the martensite continuously decreases with increasing Ti content. Fe_2Ti Laves phase starts to appear at around 4 at. % Ti and increases up to 90 vol. % at high Ti contents. The austenite fraction initially increases up to around 35 vol % at 5 at. % Ti and then decreases to around 10 vol. % at high Ti contents.

between 55 pJ and 80 pJ were used for both devices. The differences in detection rate as well as pulse frequencies between the two devices is due to the fact that the LEAP 5000 HR, in contrast to the LEAP 5000XS, features a reflectron which increases the flight path of the ions and lowers the detection efficiency of the instrument. The commercial software IVAS (version 3.8.4) was used to reconstruct the APT specimens. Voxel-based analysis was performed with a grid spacing of 1.5 nm and a delocalization of 3 nm. Specimen for APT were prepared in a FEI Helios Xe plasma focused ion beam (PFIB) – scanning electron microscope (SEM) dual-beam device by the standard lift-out process described e.g. in reference [65]. Following the lift-out, APT tips were sharpened using annular milling at 30 kV followed. Two lift-outs yielding multiple APT tips were performed in the martensitic microstructure regime number 1 at the lowest Ti content, as well as at the eutectic microstructure regime number 2 at intermediate Ti contents.

The microstructural features including different phases were highlighted in the APT reconstructed volumes by means of iso-concentration surfaces encompassing regions containing higher elemental compositions than a selected threshold value. Based on these iso-concentration surfaces, so called proximity histograms were calculated which show composition profiles as a function of the distance to the iso-concentration surface [66]. For a more accurate composition analysis, certain regions of the reconstructed APT specimens, i.e. individual microstructural features, were extracted and analyzed individually. This allowed to fine-tune the element ranges in the mass spectrum as well as to check that no artifacts such as peak overlaps of different elements were present in this region.

High-energy synchrotron X-ray diffraction (HEXRD) in transmission mode was carried out at the P07 beamline of the German Electron Synchrotron (DESY, Hamburg, Germany). The following experimental parameters were used: beam energy = 100 keV; wavelength = 0.124 Å; acquisition time = 5 s; sample-detector distance = 1626 mm; slit size = 0.5×0.5 mm^2; and an image plate detector Perkin Elmer XRD 161. A sample of $5 \times 5 \times 14$ mm^3 was cut from the graded sample with the long axis being parallel to the DED build direction (BD). The sample was investigated along the long axis from substrate to the top. Within this volume, the sample presents a variation in the Ti concentration between ~ 0 and 20 at. %. Sequences of complete Debye-Scherrer rings from the bulk of the sample (gauge volume = $5 \times 0.5 \times 0.5$ mm^3) were acquired using an image plate detector. The sample scan started from the bottom (lowest Ti concentration) and the measurements were performed with a step size of 1.0 mm down to the top of the sample (~20 at. % Ti). The instrumental parameters of the HEXRD setup were obtained using a LaB_6 powder standard (same thickness of the studied steel sample). Each HEXRD image was obtained from the sum of 10 images (exposure time/image= 0.5 s; 1 dark image/image). Quantitative phase analysis of the diffraction patterns was carried out by the Rietveld method as implemented in the software Maud [67]. For quantitative results of the HEXRD measurements, the uncertainties obtained by Rietveld analysis are displayed. An extended Williams–Imhof–Matthies–Vinel algorithm (E-WIMV) integrated in the software MAUD was used for Rietveld and texture analysis. Please see Fig. S5 in the supplementary section for an example of how the HEXRD data was analysed.

3. Results

3.1. Bulk analysis – sample overview

We produced an Fe19Ni-xTi graded specimen that allows to efficiently screen the microstructure at different compositions. The material is fully printable via DED with a relative density (averaged from 5 specimens) of 99.4 ± 0.4 % and no signs of cracks occur. Fig. 1 provides an overview of this sample and shows three different microstructure regimes that occur at low, intermediate and high Ti content. These three regimes are indicated by orange numbers and vertical orange lines in Fig. 1(a). As explained in the experimental section, etching this compositionally graded sample is difficult, which is why we complemented LOM with SEM for identifying the microstructure regimes. The microstructure of these regimes consists of: 1) at low Ti contents from 0 to 7 at. % a mainly martensitic microstructure with some retained austenite formed in a cellular dendritic solidification structure; 2) at intermediate Ti contents from 7 to 14 at. % a eutectic structure with austenite formed as primary phase from the liquid; and 3) at high Ti contents from 14 to 21 at. % a eutectic structure with Laves phase formed as primary phase from the liquid. The microstructure of these three different regimes will be discussed in more detail in Section 3.2. The locations selected for in-depth characterization (presented in Figs. 2, 3 and 4) are marked by yellow arrows in Fig. 1.

Fig. 1b shows the Ti concentration as determined by SEM-EDS along the sample height together with the corresponding Vickers hardness. It can be seen that the Ti content increases continuously, almost linearly from 0 up to 21 at. %. Between 0 and 14 at. % Ti, there is a steep increase in hardness from 300 HV to 700 HV, where the hardness reaches a plateau and does not further increase with increasing Ti concentration. Increasing the Ti content in the microstructure regimes number 1 (cellular dendritic from 0 to 7 at. %) and number 2 (first eutectic from 7 to 14 at. %) leads to a linear increase in hardness. The hardness in microstructure regime number 3 (second eutectic) is constant at 700 HV even though the Ti content increases from 14 to 21 at. %. The drop in Ti content at the very top of the sample is presumably due to a rounding off of the edge of the sample during sample preparation.

In Fig. 1c, the phase fraction of austenite (face-centered cubic, fcc), cubic martensite (body-centered cubic, bcc) and Fe_2Ti Laves phase (hexagonal) as determined by HEXRD are plotted. Initially, an increase in austenite and a decrease in martensite fraction with increasing Ti content occurs in microstructure regime number 1 (cellular dendritic). At around 4 at. % Ti, Laves phase starts to form. It increases mildly in regime number 1 and shows a steeper increase in regime number 2 (first eutectic). The steep increase in Laves phase in regime number 2 is accompanied by a steep decrease in martensite and a milder decrease in austenite. In microstructure regime number 3 (second eutectic), the phase fractions do not present significant changes. The microstructure mainly consist of Laves phase together with about 10 vol. % austenite and few vol. % of martensite.

3.2. Micro- and nano-analysis

Fig. 2 shows an in-depth characterization of the microstructure at a Ti composition of 5 at. % representative for microstructure regime number 1. The SEM micrographs and EDS mapping shown in Fig. 2a) and b) indicate a cellular dendritic solidification structure with Ti and Ni being enriched in the interdendritic regions. For this composition, HEXRD gives a phase fraction of 58 ± 5.5 vol. % martensite, 35 ± 4.0 vol. % austenite and 7 ± 1.6 vol. % Laves. Due to the high Ti content, Laves phase is preferentially etched and therefore indicated by dark areas surrounded by a bright outline in the secondary electron (SE) micrograph in Fig. 2b) as well as Fig. S1 in the supplementary section. Ni and Ti enrichment in the interdendritic regions leads to stabilization of austenite. The resulting martensitic microstructure with austenite being present at interdendritic regions is typical of AM-produced maraging steels [1,57,63,68–71]. We analyzed the microstructure of this steel composition with 5 wt. % Ti in detail in our previous publication [53] where we also demonstrated the martensitic nature of the microstructure by electron backscatter diffraction (EBSD).

APT measurements were conducted in this region containing 5 at. % Ti to obtain information on the distribution of the alloying elements at the nano-scale (see Fig. 2c)-f)). From the Ni and Ti composition found in the APT measurements, the individual measurements can be related to each phase: a high Ni and Ti content as shown in Fig. 2c) and d) indicates an APT sample origin from the austenitic interdendritic region. A lower Ni and Ti content as shown in Fig. 2e) and f) indicates an APT sample origin from a martensitic dendritic region. No precipitates or any

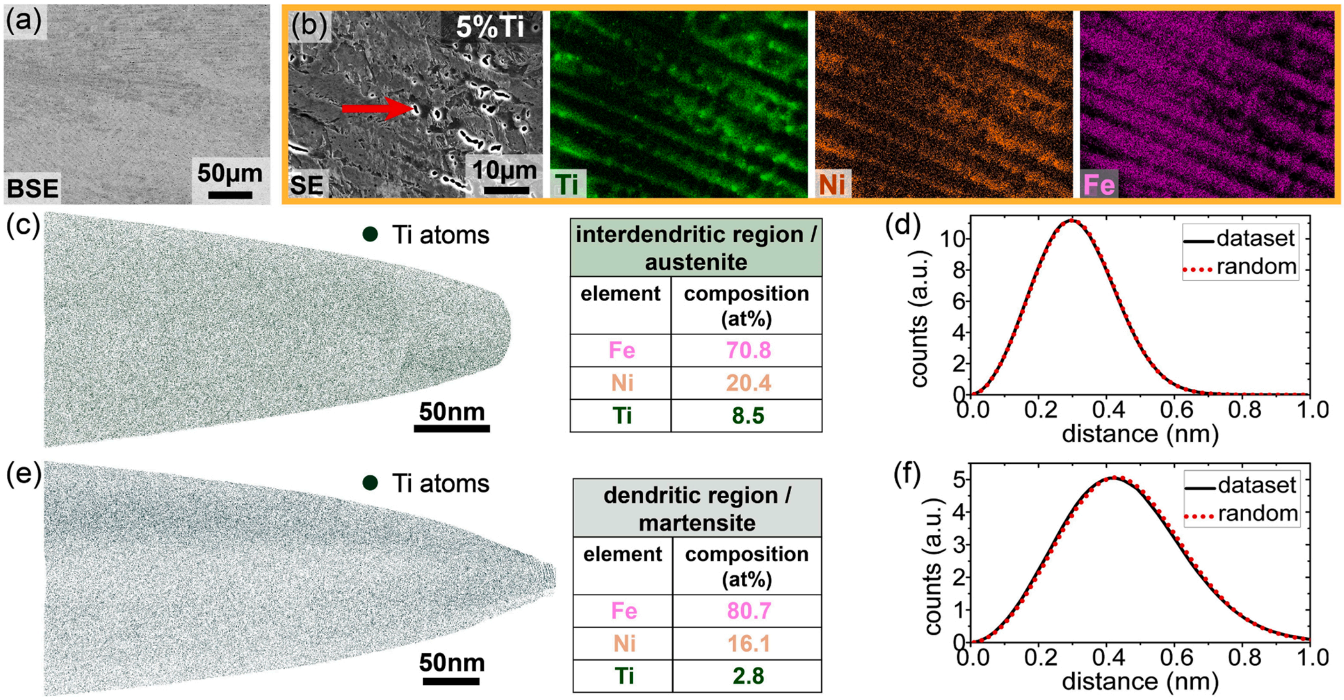

interdendritic region / austenite	
element	**composition (at%)**
Fe	70.8
Ni	20.4
Ti	8.5

dendritic region / martensite	
element	**composition (at%)**
Fe	80.7
Ni	16.1
Ti	2.8

Fig. 2. In-depth characterization of the microstructure at 5 at. % Ti composition representative for microstructure regime number 1 at low Ti content. (a) depicts a backscatter electron (BSE) micrograph at low magnification demonstrating microstructure homogeneity at large length scale. The SEM-EDS mapping in (b) visualizes the dendritic solidification structure with Ni and Ti being enriched at the interdendritic regions. A small amount of Laves phase can be seen in the SE micrograph. Because the Ti rich Laves phase is preferentially etched by Nital, it is indicated by dark regions, surrounded by bright outlines which are due to the so called "edge effect" (i.e. edges emitting high amounts of secondary electrons) in SEM. One of the Laves phase particles is marked by a red arrow. (c) and (d) show APT results from an interdendritic region, (e) and (f) from a dendritic region. Atom maps in (c) and (e) show Ti atoms in a thin slice of 5 nm thickness through the APT reconstruction. The nearest neighbor distributions in (d) and (f) demonstrate a random distribution of Ti.

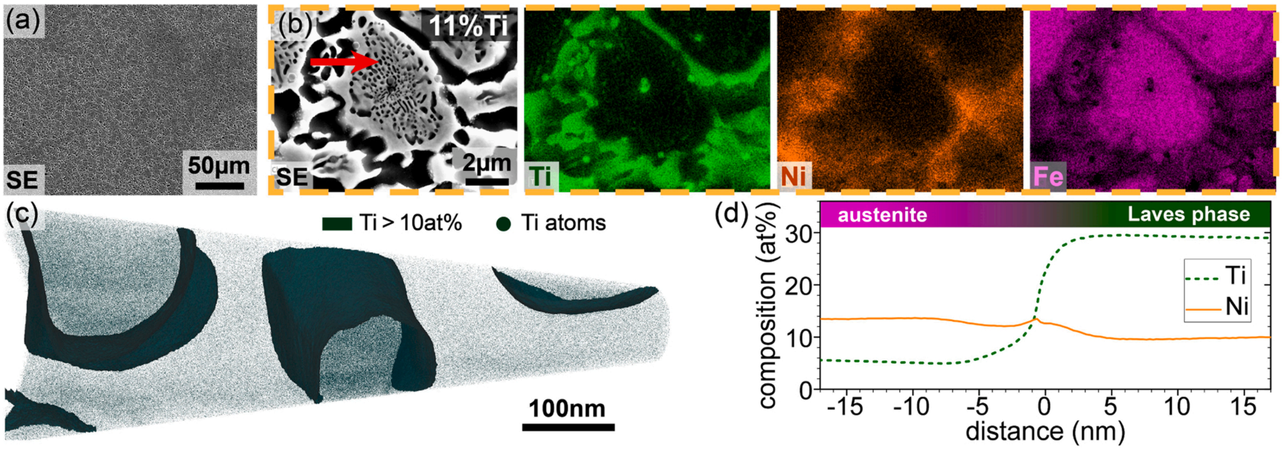

Fig. 3. In-depth characterization of the microstructure at 11 at. % Ti composition representative for microstructure regime number 2 at intermediate Ti content. (a) depicts a secondary electron (SE) micrograph at low magnification demonstrating microstructure homogeneity at large length scale. The SEM-EDS mapping in (b) visualizes the eutectic solidification structure occurring at this Ti composition. Ni and Ti are both enriched in the same regions. A region containing fine Laves phase is marked by a red arrow. (c) and (d) show APT results from such a region. For more information on APT sample preparation see Fig. S4. The atom map in (c) shows 0.5 % of the Ti atoms contained in the measured volume. Regions with Ti contents higher than 20 at. % are highlighted by a dark green iso-composition surface representing the fine Laves phase. A so-called proximity histogram, plotting the chemical composition as a function of the distance to the iso-composition surface, is shown in (d). The Laves phase contains approximately 30 at. % Ti and 10 at. % Ni, rendering it a $(Fe,Ni)_2Ti$.

irregularities in Ti distribution are visible in the so-called atom maps shown in Fig. 2c) and e) for both phases. Additionally, the nearest neighbor distributions (NND) demonstrate a perfectly random (i.e. bimodal) distribution of Ti in austenite as well as within martensite (Fig. 2d) and f)). NNDs show the distribution of distances separating each atom with its closest neighbor of the same species (i.e. Ti here). They are often used in APT analysis to identify the presence of clusters in a dataset [72]. To complement the characterization of microstructure regime number 1 (0 to 7 at. % Ti), SEM micrographs and an EDS mapping at a lower Ti content of 2 at. % are shown in Fig. S2. The lower Ti content yields a more stable solidification front which gives the microstructure a more cellular appearance compared to the more dendritic one found at 5 at. % Ti.

Fig. 3 shows a representative microstructure of microstructure

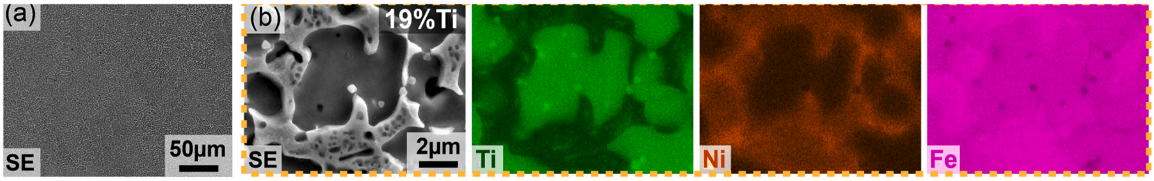

Fig. 4. In-depth characterization of the microstructure at 19 at. % Ti composition representative for microstructure regime number 3 at high Ti content. (a) depicts a secondary electron (SE) micrograph at low magnification demonstrating microstructure homogeneity at large length scale. The SEM-EDS mapping in (b) visualizes the eutectic solidification structure occurring at this Ti composition. Ni and Ti are enriched at different regions because here a different primary phase forms compared to the eutectic microstructure at intermediate Ti compositions.

regime number two at a Ti content of 11 at. %. The SEM micrographs and EDS mapping in Fig. 3a) and b) reveal the eutectic structure with Ni and Ti enriched together in one microstructural constituent: the eutectic formed by Laves phase and austenite. The region that contains less Ti and Ni is the primary austenite that presumably partially transforms into martensite upon cooling and forms some fine, secondary Laves phase. The APT reconstruction shown in Fig. 3c) contains several of these small Laves-phase particles, visualized by a dark green iso-composition surface encompassing regions of Ti content > 10 at. %. The chemical analysis of the fine Laves phase particles by means of a so-called proximity histogram shown in Fig. 3d). The composition of the Laves phase is approximately 30 at. % Ti, 10 at. % Ni and 60 at. % Fe, rendering the prototype Laves phase Fe_2Ti a $(Fe,Ni)_2Ti$ (i.e. Ni replacing some Fe). Some more details about the APT measurement within this microstructure regime can be found in Fig. S3. For this composition of 11 at. % Ti, HEXRD gives a phase fraction of 55 ± 5.6 vol. % Laves phase, 27 ± 3.3 vol. % martensite and 23 ± 3.2 vol. % austenite.

Throughout the microstructure some small Ti-oxide particles can be found. The EDS mapping in Fig. S4 a) shows the homogeneous distribution of fine oxides, while the APT measurement in Fig. S4 b) and c) demonstrates that the oxide particles mainly contain O and Ti, with few at. % Ni and C dissolved in them. These titanium oxides presumably stem from the pure titanium powder used in this study. Since Ti has a high binding affinity to oxygen, surface oxidation of the Ti powder particles is likely to occur, which carries over into the DED-deposited material.

The microstructure regime number 3 with Ti compositions from 14 to 21 at. % shows a eutectic microstructure which is different from the eutectic structure found in regime number 2. Fig. 4 shows a representative microstructure at 19 at. % Ti, demonstrating the eutectic structure. Here, the EDS mapping shows that the Ni and Ti are enriched in different regions. The Laves phase is enriched in Ti and depleted in Ni and represents the primary phase formed first during solidification. The regions in between the Laves phase are enriched in Ni (and depleted in Ti) and is presumably a mixture of Laves and austenite from the eutectic and some martensite that formed from austenite upon cooling. According to HEXRD (Fig. 1c), this region contains mainly Laves phase, 10 vol. % austenite and approximately 2 vol. % martensite. The bright spots in the Ti EDS mapping in Fig. 4 are Ti-oxide particles, just as they occur in the first eutectic regime from 7 to 14 at. % Ti and are shown in Fig. S4.

4. Discussion

The results demonstrate that the RAP concept of feeding the DED nozzle with two powders to in-situ mix the Fe19Ni (at. %) powder with pure Ti worked well. Increasing the feed rate of the Ti powder after each DED layer led to an almost linear increase in Ti composition as a function of the sample height, allowing investigation of the microstructure of a huge compositional space within a single sample.

The initial trend that the austenite fraction increases while the martensite fraction decreases upon increasing Ti content (Fig. 1c) can be rationalized by the austenite stabilizing effect of Ti. This effect of Ti was demonstrated by calculating the Gibbs Energies for austenite and martensite as a function of Ti content and related to austenite stabilization in the interdendritic regions of an Fe19Ni5Ti (at. %) steel in our previous work [53]. At around 4 at. % Ti, the formation of Laves phase starts to occur. This leads to a decrease in both austenite as well as martensite fraction in favor of Laves phase until the microstructure is mainly Laves phase at 14 at. % Ti. Further Ti increase does not change the phase fractions significantly.

As demonstrated in Fig. 5, the microstructures found in the different regimes can be explained using the phase diagram of the Fe19Ni-xTi (at. %) alloy system. In microstructure regime number 1, solidification starts with fcc austenite. The alloying elements Ni and Ti are rejected into the liquid phase where they enrich the interdendritic regions during progressing solidification. As both Ni and Ti act as austenite stabilizers in this system [53,73,74], the austenite is stabilized in these regions at room temperature. In the first layer of the DED specimen, at 0 at. % Ti, approximately 3 vol. % austenite occurs. The more Ti is added, the more pronounced this microsegregation becomes and the more austenite is stabilized in the interdendritic regions. At a composition of 4 at. % Ti, fine Laves phase particles begin to be formed in the regions of highest Ti content in the interdendritic regions.

In regime number 2 of intermediate Ti composition, solidification still starts with fcc austenite being the primary phase to form. Ni and Ti are enriched in the remaining liquid until the eutectic composition is reached (which is higher than the bulk Ti composition in this regime) and eutectic solidification takes place. In contrast, in microstructure regime number 3, solidification starts from the opposite side of the eutectic concentration. Laves phase is formed as the primary phase, incorporating Ti and only partitioning Ni to the liquid phase. When the eutectic composition is reached (which is lower than the bulk Ti composition in this regime) the remaining liquid solidifies eutectically [73]. Consequently, the border between microstructure regime number 2 and 3 is expected to occur exactly at the eutectic composition of 15 at. % Ti (see phase diagram in Fig. 5). This fits well to the border determined experimentally in Section 3.1. from Fig. 1 at 14 at. % Ti. The equilibrium phase diagram shown in Fig. 5 is well suited to explain the phases and the complex microstructures formed during DED. Additionally, solidification phenomena can explain further details of the microstructures observed. The change from microstructure regime number 1 to number 2 occurs at the transition of columnar dendritic to equiaxed dendritic [75]. This transition occurs due to a combined effect of reduced temperature gradient as a consequence of the heating up of the sample [4,45,76] and a higher undercooling due to a higher alloying element (i.e., Ti) content and more pronounced microsegregation. The constitutional undercooling is altered by the chemical composition.

A fine microstructure, characteristic for the rapid solidification during laser additive manufacturing [1,20,57,63], is observed in all three microstructure regimes. Feature sizes in the range of 3 to 6 μm for the primary dendrite arm spacing can be found in the first microstructure regime, which is the most important one for this study as it produces the martensitic microstructure desired for a maraging steel [60]. The primary austenite phase size in regime number 2 and the primary Laves phase size in the microstructure regime 3 are in the range of 4 to 10 μm.

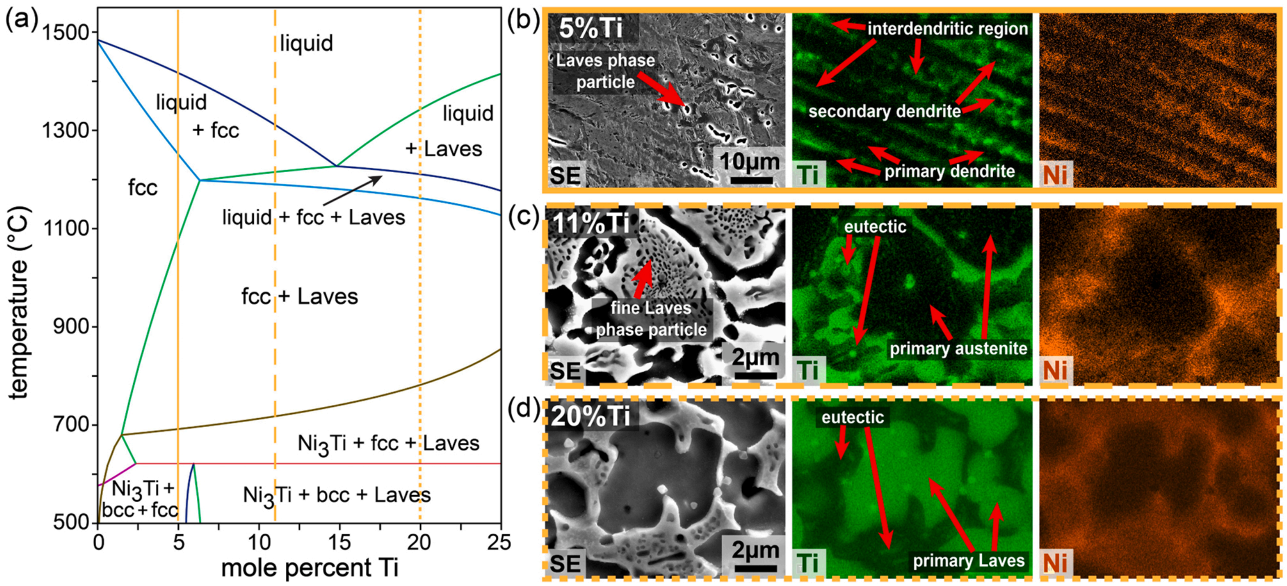

Fig. 5. Thermodynamic simulations together with representative microstructures occurring at different Ti compositions on the DED produced compositionally graded sample. (a) shows a pseudo-binary phase diagram for the Fe19Ni-xTi (at. %) alloy. The phase diagram was calculated using the Thermo-Calc software in conjunction with the TCFE7 database. The solid, dashed and dotted orange lines mark the Ti composition of the corresponding microstructures shown on the right side. (b)-(d) depicts the EDS mappings of Ni and Ti from the three microstructure regimes presented in the results section in Figs. 2–4.

The increase in hardness from 300 HV to 500 HV in the first microstructure regime is due to a combination of multiple effects: solid solution hardening with an increasing amount of Ti and dispersion with an increasing amount of austenite as well as Laves phase. The further increase in hardness up to 700 HV is due to a complex interplay, namely a decrease of the soft austenite phase and an increase of the hard Laves phase. However, as can be seen in Fig. 3, all these phases occur in different sizes and morphologies which makes it difficult to estimate their individual contributions to the overall hardness. The hardness plateau at 700 HV in the third microstructure regime is not surprising as the phase fractions do not change significantly here despite the increasing Ti content. Apparently, solid solution strengthening plays a minor role at these higher Ti contents and in their complex, multi-phase microstructure.

As explained in the introduction section, one would expect pronounced in-situ precipitation of fine Ni_3Ti η-phase in microstructure regime number 1 featuring the cellular dendritic solidification structure similar to that reported in previous research on an Fe19Ni-xAl (at. %) alloy [35]. However, APT shows that the distribution of Ti is random (see Fig. 2c) and e)) and no η-phase precipitates occur in this microstructure regime. No precipitates were triggered by the IHT in this sample, despite the expected fast precipitation kinetics of the Fe-Ni-Ti system, the pronounced heat input from the laser during DED, and the successful achievement of the cellular dendritic solidification structure overlaid with the mainly martensitic microstructure. This fact can be understood through a closer examination of the time-temperature profile imposed during the DED process. In a previous study [53], we used exactly the composition of microstructure regime number 1 still featuring the mainly martensitic microstructure. We showed that via controlling the temperature during the deposition of each individual DED layer, just before IHT from the subsequent layer, it is possible to control whether in-situ precipitation occurs in an Fe19Ni5Ti (wt. %) steel or not. During the DED process, the (base) temperature of sample and substrate increase rapidly due to the continuous heat input from the laser. This leads to an increase of the temperature above the martensite start temperature M_s which is 195 °C for an Fe19Ni5Ti (wt. %) steel [53]. Consequently, the deposited material remains austenitic during the build of the sample. In this case, the IHT from subsequent layers cannot trigger η-phase precipitation as there is no driving force for precipitation in austenite, only in martensite. In-situ precipitation hardening can only be obtained if the material cools below M_s before the IHT of the next layer is applied. Understanding this sequence of phase transformations permits to locally modify the microstructure: locally keeping the temperature above M_s during the build avoids precipitation while locally cooling below M_s allows in-situ precipitation hardening in this region. The newly designed Fe-Ni-Ti maraging steel has a M_s temperature which is readily accessible during DED without prolonged cooling intervals.

In our above mentioned previously published research [53] where we used the composition identified here as still featuring a martensitic microstructure in regime number 1, we analyzed the mechanical properties. If the process is designed in a way such that the IHT can trigger Ni_3Ti η-phase precipitation, microstructure regime 1 at a composition of Fe19Ni5Ti (wt. %) can yield a tensile strength of 1300 MPa at an elongation of 10 % [53]. These mechanical properties are quite impressive considering the simple ternary alloy and the fact that no post-process heat treatment was applied. A DED produced Fe17Ni10Al (at. %) steel showed an even higher tensile strength of 1550 MPa but lower elongation of only 3.5 % after in-situ precipitation hardening with fine NiAl precipitates [77]. From an alloy design perspective, it seems interesting to study in future also the quaternary Fe-Ni-Al-Ti system and specifically screen the compositional space up to 10 at. % Al and up to 5 at. % Ti. This way it might be possible to combine in-situ NiAl- with Ni_3Ti-precipitation in the desired cellular dendritic / martensitic microstructure to obtain material variants with excellent combinations of high yield strength and elongation. Furthermore, we propose to study the microstructure of regime number 2 in more detail regarding achievable mechanical properties. The high hardness up to 700 HV together with the fine microstructure found at this intermediate Ti composition from 7 to 14 at. % appears to be very promising for future studies.

5. Conclusions

In this study we demonstrated the design of a novel, plain, ternary Fe-Ni-Ti maraging steel optimized for laser additive manufacturing (LAM). The following conclusions can be drawn:

- The rapid alloy prototyping approach to use a compositionally graded specimen to screen a wide compositional space from 0 to 21 at. % Ti on a single sample worked well and is very efficient. In the region from 0 to 7 at. % Ti, the desired martensitic microstructure (overlaid on a cellular dendritic solidification structure) was obtained. Additionally, two different microstructures containing a eutectic structure were identified within the regions 7 to 14 at. % Ti and 14 to 21 at. % Ti.
- The alloying elements are distributed randomly in the desired mainly martensitic microstructure, i.e. no in-situ precipitation of supersaturated Ti is taking place in this study. This is due to the fact, that the material has not transformed to martensite at the time of IHT as we demonstrated in our previous study [53]. Controlling whether precipitation occurs or not, allows to use the newly developed Fe-Ni-Ti steel in the composition range up to 7 at. % Ti to locally adjust the microstructure and consequently the mechanical properties of LAM-produced parts to desired requirements.
- Despite the inherently dynamic DED process, characterized by high heating and cooling rates, the phases found in the microstructures for the different alloy compositions can be identified with the help of the equilibrium phase diagrams, calculated by Calphad.

CRediT authorship contribution statement

Philipp Kürnsteiner: Writing – review & editing, Writing – original draft, Visualization, Methodology, Investigation, Formal analysis, Data curation, Conceptualization. **Pere Barriobero-Vila:** Writing – review & editing, Visualization, Validation, Investigation, Formal analysis. **Priyanshu Bajaj:** Writing – review & editing, Visualization, Investigation. **Frédéric De Geuser:** Writing – review & editing, Visualization, Investigation, Formal analysis. **Markus B. Wilms:** Writing – review & editing, Methodology, Investigation, Conceptualization. **Eric A. Jägle:** Writing – review & editing, Supervision, Methodology, Funding acquisition, Formal analysis, Conceptualization. **Dierk Raabe:** Writing – review & editing, Supervision, Funding acquisition, Conceptualization.

Declaration of Competing Interest

The authors declare that they have no known competing financial interests or personal relationships that could have appeared to influence the work reported in this paper.

Data Availability

Data will be made available on request.

Acknowledgments

This work was carried out in the scope of the AProLAM project, funded jointly by the Fraunhofer Society, Germany and the Max Planck Society, Germany in their strategic cooperation framework. The authors acknowledge the help of Baptiste Gault with APT data analysis. The authors are grateful to Uwe Tezins and Andreas Sturm for their support to the FIB and APT facilities at MPIE. Heidi Bögershausen and Marco Hoff are acknowledged for their help with sample preparation for optical microscopy and hardness measurements. P.K. gratefully acknowledges the financial support by the Austrian Federal Ministry for Digital and Economic Affairs, the National Foundation for Research, Technology and Development, Austria and the Christian Doppler Research Association, Austria. P.B.-V. acknowledges financial support from the Spanish Ministry of Science through the Ramón y Cajal grant RYC2020-029585-I.

Appendix A. Supporting information

Supplementary data associated with this article can be found in the online version at doi:10.1016/j.addma.2023.103647.

References

[1] D. Herzog, V. Seyda, E. Wycisk, C. Emmelmann, Additive manufacturing of metals, Acta Mater. 117 (2016) 371–392, https://doi.org/10.1016/j.actamat.2016.07.019.

[2] W.E. Frazier, Metal additive manufacturing: a review, J. Mater. Eng. Perform. 23 (2014) 1917–1928, https://doi.org/10.1007/s11665-014-0958-z.

[3] D.D. Gu, W. Meiners, K. Wissenbach, R. Poprawe, Laser additive manufacturing of metallic components: materials, processes and mechanisms, Int. Mater. Rev. 57 (2012) 133–164, https://doi.org/10.1179/1743280411Y.0000000014.

[4] F. Spranger, B. Graf, M. Schuch, K. Hilgenberg, M. Rethmeier, Build-up strategies for additive manufacturing of three dimensional Ti-6Al-4V-parts produced by laser metal deposition, J. Laser Appl. 30 (2018), 022001, https://doi.org/10.2351/1.4997852.

[5] A. Gasser, G. Backes, I. Kelbassa, A. Weisheit, K. Wissenbach, Laser additive manufacturing: laser metal deposition (LMD) and selective laser melting (SLM) in turbo-engine applications, Laser Material Processing. (2010) 58–63. https://doi.org/10.1002/latj.201090029.

[6] R. Liu, Z. Wang, T. Sparks, F. Liou, J. Newkirk, Aerospace applications of laser additive manufacturing, in: Laser Additive Manufacturing: Materials, Design, Technologies, and Applications, Elsevier Inc., 2017: pp. 351–371. https://doi.org/10.1016/B978–0-08–100433-3.00013–0.

[7] K. Tan, S. Markovych, W. Hu, O. Shorinov, Y. Wang, Review of manufacturing and repair of aircraft and engine parts based on cold spraying technology and additive manufacturing technology, Aerosp. Tech. Technol. (2020) 53–70, https://doi.org/10.32620/aktt.2020.3.06.

[8] A. Boschetto, L. Bottini, V. Cardini, M. Eugeni, P. Gaudenzi, F. Veniali, Aircraft part substitution via additive manufacturing: design, simulation, fabrication and testing, Rapid Prototyp. J. (2021), https://doi.org/10.1108/RPJ-06-2020-0140.

[9] I. Kelbassa, A. Gasser, K. Wissenbach, Laser cladding as a repair technique for BLISKs out of titanium and nickel base alloys used in aero engines, Pacific International Conference on Applications of Lasers and Optics. 2004 (2018) 503. https://doi.org/10.2351/1.5056104.

[10] S.L. Campanelli, N. Contuzzi, A. Angelastro, A.D. Ludovico, Capabilities and performances of the selective laser melting process, in: M.J. Er (Ed.), New Trends in Technologies: Devices, Computer, Communication and Industrial Systems, Sciyo, 2012: pp. 233–252. https://doi.org/10.5772/10432.

[11] A. Armillotta, R. Baraggi, S. Fasoli, SLM tooling for die casting with conformal cooling channels, Int. J. Adv. Manuf. Technol. 71 (2014) 573–583, https://doi.org/10.1007/s00170-013-5523-7.

[12] S. Kumar, S. Pityana, Laser-based additive manufacturing of metals, Adv. Mater. Res. 227 (2011) 92–95, https://doi.org/10.4028/www.scientific.net/AMR.227.92.

[13] M. Mazur, P. Brincat, M. Leary, M. Brandt, Numerical and experimental evaluation of a conformally cooled H13 steel injection mould manufactured with selective laser melting, Int. J. Adv. Manuf. Technol. 93 (2017) 881–900, https://doi.org/10.1007/s00170-017-0426-7.

[14] R. Galante, C.G. Figueiredo-Pina, A.P. Serro, Additive manufacturing of ceramics for dental applications: a review, Dent. Mater. 35 (2019) 825–846, https://doi.org/10.1016/j.dental.2019.02.026.

[15] L.E. Murr, Additive manufacturing of biomedical devices: an overview, Mater. Technol. 33 (2018) 57–70, https://doi.org/10.1080/10667857.2017.1389052.

[16] H. Lei, T. Yi, H. Fan, X. Pei, L. Wu, F. Xing, M. Li, L. Liu, C. Zhou, Y. Fan, X. Zhang, Customized additive manufacturing of porous Ti6Al4V scaffold with micro-topological structures to regulate cell behavior in bone tissue engineering, Mater. Sci. Eng. C 120 (2021), https://doi.org/10.1016/j.msec.2020.111789.

[17] T. Niendorf, F. Brenne, P. Hoyer, D. Schwarze, M. Schaper, R. Grothe, M. Wiesener, G. Grundmeier, H.J. Maier, Processing of new materials by additive manufacturing: iron-based alloys containing silver for biomedical applications, Metall. Mater. Trans. A 46 (2015) 2829–2833, https://doi.org/10.1007/s11661-015-2932-2.

[18] N. Guo, M.C. Leu, Additive manufacturing: technology, applications and research needs, Front. Mech. Eng. 8 (2013) 215–243, https://doi.org/10.1007/s11465-013-0248-8.

[19] J.H. Martin, B.D. Yahata, J.M. Hundley, J.A. Mayer, T.A. Schaedler, T.M. Pollock, 3D printing of high-strength aluminium alloys, Nature 549 (2017) 365–369, https://doi.org/10.1038/nature23894.

[20] Y.M. Wang, T. Voisin, J.T. McKeown, J. Ye, N.P. Calta, Z. Li, Z. Zeng, Y. Zhang, W. Chen, T.T. Roehling, R.T. Ott, M.K. Santala, P.J. Depond, M.J. Matthews, A. v Hamza, T. Zhu, Additively manufactured hierarchical stainless steels with high strength and ductility, Nat. Mater. (2017), https://doi.org/10.1038/nmat5021.

[21] N. Kaufmann, M. Imran, T.M. Wischeropp, C. Emmelmann, S. Siddique, F. Walther, Influence of process parameters on the quality of aluminium alloy EN AW 7075 using selective laser melting (SLM), Phys. Procedia 83 (2016) 918–926, https://doi.org/10.1016/j.phpro.2016.08.096.

[22] European Commisison, Final Report Summary - HI-STA-PART (High Strength Aluminium Alloy Parts by Selective Laser Melting), (2016) 1–5. http://cordis.europa.eu/result/rcn/177612_en.html.

[23] R. Mertens, S. Dadbakhsh, J. van Humbeeck, J.-P. Kruth, Application of base plate preheating during selective laser melting, Procedia CIRP 74 (2018) 5–11, https://doi.org/10.1016/j.procir.2018.08.002.

[24] S.C. Altıparmak, V.A. Yardley, Z. Shi, J. Lin, Challenges in additive manufacturing of high-strength aluminium alloys and current developments in hybrid additive manufacturing, Int. J. Lightweight Mater. Manuf. 4 (2021) 246–261, https://doi.org/10.1016/j.ijlmm.2020.12.004.

[25] Y. He, M. Zhong, J. Beuth, B. Webler, A study of microstructure and cracking behavior of H13 tool steel produced by laser powder bed fusion using single-tracks, multi-track pads, and 3D cubes, J. Mater. Process. Technol. 286 (2020), https://doi.org/10.1016/j.jmatprotec.2020.116802.

[26] A. Singh, A. Ramakrishnan, G.P. Dinda, Direct Laser Metal Deposition of Eutectic Al-Si Alloy for Automotive Applications, in: TMS 2017 146th Annual Meeting & Exhibition Supplemental Proceedings, 2017: pp. 71–80. https://doi.org/10.1007/978-3-319-51493-2.

[27] W. Pei, W. Zhengying, C. Zhen, D. Jun, H. Yuyang, L. Junfeng, Z. Yatong, The AlSi10Mg samples produced by selective laser melting single track densification microstructure and mechanical behavior, Appl. Surf. Sci. 408 (2017) 38–50, https://doi.org/10.1016/j.apsusc.2017.02.215.

[28] A. bin Anwar, Q.C. Pham, Selective laser melting of AlSi10Mg: Effects of scan direction, part placement and inert gas flow velocity on tensile strength, J. Mater. Process. Technol. 240 (2017) 388–396, https://doi.org/10.1016/j.jmatprotec.2016.10.015.

[29] P. Ma, K. Prashanth, S. Scudino, Y. Jia, H. Wang, C. Zou, Z. Wei, J. Eckert, Influence of annealing on mechanical properties of Al-20Si processed by selective laser melting, Metals 4 (2014) 28–36, https://doi.org/10.3390/met4010028.

[30] E.O. Olakanmi, R.F. Cochrane, K.W. Dalgarno, A review on selective laser sintering/melting (SLS/SLM) of aluminium alloy powders: processing, microstructure, and properties, Prog. Mater. Sci. 74 (2015) 401–477, https://doi.org/10.1016/j.pmatsci.2015.03.002.

[31] A. Yadollahi, N. Shamsaei, S.M. Thompson, D.W. Seely, Effects of process time interval and heat treatment on the mechanical and microstructural properties of direct laser deposited 316L stainless steel, Mater. Sci. Eng.: A 644 (2015) 171–183, https://doi.org/10.1016/j.msea.2015.07.056.

[32] Y. Zhang, G. Yu, X. He, Numerical study of thermal history in laser aided direct metal deposition process, Sci. China.: Phys., Mech. Astron. 55 (2012) 1431–1438, https://doi.org/10.1007/s11433-012-4793-7.

[33] B. Zheng, Y. Zhou, J.E. Smugeresky, J.M. Schoenung, E.J. Lavernia, Thermal behavior and microstructural evolution during laser deposition with laser-engineered net shaping: Part I. Numerical calculations, Metall. Mater. Trans. A: Phys. Metall. Mater. Sci. 39 (2008) 2228–2236, https://doi.org/10.1007/s11661-008-9557-7.

[34] P. Krakhmalev, I. Yadroitsava, G. Fredriksson, I. Yadroitsev, In situ heat treatment in selective laser melted martensitic AISI 420 stainless steels, Mater. Des. 87 (2015) 380–385, https://doi.org/10.1016/j.matdes.2015.08.045.

[35] P. Kürnsteiner, M.B. Wilms, A. Weisheit, P. Barriobero-Vila, E.A. Jägle, D. Raabe, Massive nanoprecipitation in an Fe-19Ni-xAl maraging steel triggered by the intrinsic heat treatment during laser metal deposition, Acta Mater. 129 (2017) 52–60, https://doi.org/10.1016/j.actamat.2017.02.069.

[36] P. Kürnsteiner, M.B. Wilms, A. Weisheit, P. Barriobero-Vila, B. Gault, E.A. Jägle, D. Raabe, In-process precipitation during laser additive manufacturing investigated by atom probe tomography, Microsc. Microanal. 23 (2017) 694–695, https://doi.org/10.1017/S1431927617004135.

[37] A. Seidel, S. Saha, T. Maiwald, J. Moritz, S. Polenz, A. Marquardt, J. Kaspar, T. Finaske, E. Lopez, F. Brueckner, C. Leyens, Intrinsic heat treatment within additive manufacturing of gamma titanium aluminide space hardware, JOM 71 (2019) 1513–1519, https://doi.org/10.1007/s11837-019-03382-2.

[38] J. Damon, R. Koch, D. Kaiser, G. Graf, S. Dietrich, V. Schulze, Process development and impact of intrinsic heat treatment on the mechanical performance of selective laser melted AISI 4140, Addit. Manuf. 28 (2019) 275–284, https://doi.org/10.1016/j.addma.2019.05.012.

[39] S. Amirabdollahian, F. Deirmina, L. Harris, R. Siriki, M. Pellizzari, P. Bosetti, A. Molinari, Towards controlling intrinsic heat treatment of maraging steel during laser directed energy deposition, Scr. Mater. 201 (2021), https://doi.org/10.1016/j.scriptamat.2021.113973.

[40] H. Yang, J. Yang, W. Huang, G. Jing, Z. Wang, X. Zeng, Controllable in-situ aging during selective laser melting: Stepwise precipitation of multiple strengthening phases in Inconel 718 alloy, J. Mater. Sci. Technol. 35 (2019) 1925–1930, https://doi.org/10.1016/j.jmst.2019.05.024.

[41] J. Haubrich, J. Gussone, P. Barriobero-Vila, P. Kürnsteiner, E.A. Jägle, D. Raabe, N. Schell, G. Requena, The role of lattice defects, element partitioning and intrinsic heat effects on the microstructure in selective laser melted Ti-6Al-4V, Acta Mater. 167 (2019) 136–148, https://doi.org/10.1016/j.actamat.2019.01.039.

[42] W. Xu, M. Brandt, S. Sun, J. Elambasseril, Q. Liu, K. Latham, K. Xia, M. Qian, Additive manufacturing of strong and ductile Ti-6Al-4V by selective laser melting via in situ martensite decomposition, Acta Mater. 85 (2015) 74–84, https://doi.org/10.1016/j.actamat.2014.11.028.

[43] W. Xu, S. Sun, J. Elambasseril, Q. Liu, M. Brandt, M. Qian, Ti-6Al-4V additively manufactured by selective laser melting with superior mechanical properties, Jom 67 (2015) 668–673, https://doi.org/10.1007/s11837-015-1297-8.

[44] H.Z. Zhong, M. Qian, W. Hou, X.Y. Zhang, J.F. Gu, The β phase evolution in Ti-6Al-4V additively manufactured by laser metal deposition due to cyclic phase transformations, Mater. Lett. 216 (2018) 50–53, https://doi.org/10.1016/j.matlet.2017.12.140.

[45] P. Kürnsteiner, P. Bajaj, A. Gupta, M.B. Wilms, A. Weisheit, X. Li, C. Leinenbach, B. Gault, E.A. Jägle, D. Raabe, Control of thermally stable core-shell nano-precipitates in additively manufactured Al-Sc-Zr alloys, Addit. Manuf. 32 (2020), 100910, https://doi.org/10.1016/j.addma.2019.100910.

[46] Z. Wang, X. Lin, N. Kang, J. Chen, Y. Tang, H. Tan, X. Yu, H. Yang, W. Huang, Directed energy deposition additive manufacturing of a Sc/Zr-modified Al–Mg alloy: Effect of thermal history on microstructural evolution and mechanical properties, Mater. Sci. Eng. A 802 (2021), https://doi.org/10.1016/j.msea.2020.140606.

[47] C. Tan, K. Zhou, W. Ma, P. Zhang, M. Liu, T. Kuang, Microstructural evolution, nanoprecipitation behavior and mechanical properties of selective laser melted high-performance grade 300 maraging steel, Mater. Des. 134 (2017) 23–34, https://doi.org/10.1016/j.matdes.2017.08.026.

[48] J. Mazumder, J. Choi, K. Nagarathnam, J. Koch, D. Hetzner, The direct metal deposition of H13 tool steel for 3-D components, JOM 49 (1997) 55–60.

[49] R. Cottam, J. Wang, V. Luzin, Characterization of microstructure and residual stress in a 3D H13 tool steel component produced by additive manufacturing, J. Mater. Res. 29 (2014) 1978–1986, https://doi.org/10.1557/jmr.2014.190.

[50] E.V. Pereloma, R.A. Stohr, M.K. Miller, S.P. Ringer, Observation of precipitation evolution in Fe-Ni-Mn-Ti-Al maraging steel by atom probe tomography, Metall. Mater. Trans. A: Phys. Metall. Mater. Sci. 40 (2009) 3069–3075, https://doi.org/10.1007/s11661-009-9993-z.

[51] A. Shekhter, H.I. Aaronson, M.K. Miller, S.P. Ringer, E.V. Pereloma, Effect of aging and deformation on the microstructure and properties of Fe-Ni-Ti maraging steel, Metall. Mater. Trans. A: Phys. Metall. Mater. Sci. 35 (2004) 973–983, https://doi.org/10.1007/s11661-004-1001-z.

[52] E.V. Pereloma, A. Shekhter, M.K. Miller, S.P. Ringer, Ageing behaviour of an Fe-20Ni-1.8Mn-1.6Ti-0.59Al (wt%) maraging alloy: clustering, precipitation and hardening, Acta Mater. 52 (2004) 5589–5602, https://doi.org/10.1016/j.actamat.2004.08.018.

[53] P. Kürnsteiner, M.B. Wilms, A. Weisheit, B. Gault, E.A. Jägle, D. Raabe, High-strength Damascus steel by additive manufacturing, Nature 582 (2020) 515–519, https://doi.org/10.1038/s41586-020-2409-3.

[54] R.F. Decker, Source Book on Maraging Steels, American Society for Metals International, Metals Park, OH, 1979.

[55] R.F. Decker, J.T. Eash, A.J. Goldman, 18% Nickel maraging steel, Trans. ASM 55 (1962) 58–76.

[56] W. Sha, Z. Guo, Maraging steels: modelling of microstructure, properties and applications, CRC Press, New York, 2009. https://doi.org/10.1533/9781845696931.142.

[57] P. Bajaj, A. Hariharan, A. Kini, P. Kürnsteiner, D. Raabe, E.A. Jägle, Steels in additive manufacturing: a review of their microstructure and properties, Mater. Sci. Eng.: A 772 (2020), 138633, https://doi.org/10.1016/j.msea.2019.138633.

[58] S. Bodziak, K.S. Al-Rubaie, L.D. Valentina, F.H. Lafratta, E.C. Santos, A.M. Zanatta, Y. Chen, Precipitation in 300 grade maraging steel built by selective laser melting: aging at 510 °C for 2h, Mater. Charact. 151 (2019) 73–83, https://doi.org/10.1016/j.matchar.2019.02.033.

[59] W. Sha, A. Cerezo, G.D.W. Smith, Phase chemistry and precipitation reactions in maraging steels: Part IV. Discussion and conclusions, Metall. Trans. A 24 (1993) 1251–1256, https://doi.org/10.1007/BF02668193.

[60] W. Sha, Z. Guo, Maraging Steels, Woodhead Publishing, 2009, https://doi.org/10.1533/9781845696931.

[61] M.N. Rao, Progress in understanding the metallurgy of 18% nickel maraging steels, Int. J. Mater. Res. 97 (2006) 1594–1607.

[62] E.A. Jägle, Z. Sheng, P. Kürnsteiner, S. Ocylok, A. Weisheit, D. Raabe, Comparison of maraging steel micro- and nanostructure produced conventionally and by laser additive manufacturing, Materials 10 (2017), https://doi.org/10.3390/ma10010008.

[63] S.L. Campanelli, A. Angelastro, C.G. Signorile, G. Casalino, Investigation on direct laser powder deposition of 18 Ni (300) marage steel using mathematical model and experimental characterisation (2017) 885–895, https://doi.org/10.1007/s00170-016-9135-x.

[64] H. Knoll, S. Ocylok, A. Weisheit, H. Springer, E. Jägle, D. Raabe, Combinatorial alloy design by laser additive manufacturing, Steel Res. Int. 88 (2017) 1–11, https://doi.org/10.1002/srin.201600416.

[65] D.J. Larson, T.J. Prosa, R.M. Ulfig, B.P. Geiser, T.F. Kelly, Local Electrode Atom Probe Tomography: A User's Guide, Springer, New York, 2013, https://doi.org/10.1007/978-1-4614-8721-0.

[66] O.C. Hellman, J.A. Vandenbroucke, J. Rüsing, D. Isheim, D.N. Seidman, Analysis of three-dimensional atom-probe data by the proximity histogram, Microsc. Microanal. 6 (2019) 437–444, https://doi.org/10.1007/s100050010051.

[67] L. Lutterotti, S. Matthies, H.R. Wenk, A.S. Schultz, J.W. Richardson, Combined texture and structure analysis of deformed limestone from time-of-flight neutron diffraction spectra, J. Appl. Phys. 81 (1997) 594–600, https://doi.org/10.1063/1.364220.

[68] C. Tan, K. Zhou, M. Kuang, W. Ma, T. Kuang, Microstructural characterization and properties of selective laser melted maraging steel with different build directions, Sci. Technol. Adv. Mater. 19 (2018) 746–758, https://doi.org/10.1080/14686996.2018.1527645.

[69] T. Becker, D. Dimitrov, The achievable mechanical properties of SLM produced maraging Steel 300 components, Rapid Prototyp. J. 22 (2016) 487–494, https://doi.org/10.1108/RPJ-08-2014-0096.

[70] K. Kempen, E. Yasa, L. Thijs, J.P. Kruth, J. van Humbeeck, Microstructure and mechanical properties of selective laser melted 18Ni-300 steel, Phys. Procedia 12 (2011) 255–263, https://doi.org/10.1016/j.phpro.2011.03.033.

[71] E.A. Jägle, Z. Sheng, P. Kürnsteiner, S. Ocylok, A. Weisheit, D. Raabe, Comparison of maraging steel micro- and nanostructure produced conventionally and by laser additive manufacturing, Materials 10 (2017), https://doi.org/10.3390/ma10010008.

[72] B. Gault, M.P. Moody, J.M. Cairney, S.P. Ringer, Atom Probe Microscopy, Springer Verlag, New York, 2012.

[73] D.A. Porter, K.E. Eastering, Phase Transformation in Metals and Alloys, Springer-Science+Business Media, 1992.

[74] M. Durand-Charre, Microstructure of Steels and Cast Irons, Springer, 2004.

[75] D.M. Stefanescu, R. Roxana, Fundamentals of solidification, in: Fundamentals of Solidification, Trans Tech Publications, 1986 https://doi.org/AR1RAAAAMAAJ.

[76] Z. Wang, T.A. Palmer, A.M. Beese, Effect of processing parameters on microstructure and tensile properties of austenitic stainless steel 304L made by directed energy deposition additive manufacturing, Acta Mater. 110 (2016) 226–235, https://doi.org/10.1016/j.actamat.2016.03.019.

[77] P. Kürnsteiner, Precipitation Reactions During the Intrinsic Heat Treatment of Laser Additive Manufacturing (2019), https://doi.org/10.18154/RWTH-2019-11831.